PHYSICAL REVIEW B VOLUME 7, NUMBER 8 15 APRIL 1973

Infrared-Reflectance Spectra of Layered Group-IV and Group-VI Transition-Metal Dichalcogenides

G. Lucovsky and R. M. White
Xerox Palo Alto Research Center, Palo Alto, California 94304

J. A. Benda* and J. F. Revelli*
Department of Applied Physics, Stanford University, Palo Alto, California 94304

(Received 5 October 1972)

Infrared-reflectivity spectra have been obtained for a large number of group-IV (Ti, Zr, Hf) and group-VI (Mo, W) transition-metal dichalcogenides. Three distinct types of spectra have been identified: In ZrS_2, HfS_2, and $HfSe_2$, very strong reststrahlen with effective charges $e_T^* \sim 4e$; in MoS_2, $MoSe_2$, WS_2, and WSe_2, weaker reststrahlen with $e_T^* \sim 0.5e$; and in TiS_2, $ZrTe_2$, and $HfTe_2$, plasmon-type reflection bands corresponding to free-carrier densities in excess of $10^{20}/cm^3$. These observations, coupled with considerations of ion size, have led to a new description of the chemical bonding in these layered materials that is not consistent with a simple rigid-band scheme.

I. INTRODUCTION

Recently, there has been an upsurge of interest in layered crystals, particularly the transition-metal dichalcogenides where intercalation of alkali-metal atoms or organic molecules can lead to increases in the critical temperature for superconductivity.[1,2] To date there have been a limited number of studies of the long-wavelength infrared- and Raman-active optic vibrational modes.[3-7] The emphasis in these studies has been on the differences in the intralayer and interlayer forces. Zallen, Slade, and Ward[3] studied the layered crystals As_2S_3 and As_2Se_3 and demonstrated by means of a combination of Raman and infrared results that the diperiodic symmetry of the individual layers was dominant, and that weaker interlayer interactions were observable as small splittings between Raman-infrared Davydov doublets. The characteristic splittings were of the order of 2%, so that the interlayer forces were approximately 100 times smaller than the intralayer forces. Wieting and Verble[4] studied the infrared- and Raman-active modes of hexagonal (2*H*) MoS_2, and from the near degeneracy of the E_{1u} and E_{2g}^1 modes they concluded a very weak interlayer interaction with respect to shear. The same authors also studied β-GaSe [5] and concluded that there was electrostatic as well as Van der Waals coupling between the layers. Smith and co-workers [6,7] studied the Raman spectra of the disulfides and diselenides of Zr, Hf, and Ti and found that the Raman frequencies were relatively insensitive to the identity of the metal ion. They also studied the infrared reflectance of HfS_2 and noted that the LO-TO splitting in that crystal was substantially larger than in MoS_2, indicating a greater degree of ionicity in the hafnium compound.

In this paper the emphasis is on the strength of the infrared-active modes, which, when related to an effective charge parameter, gives information about the intralayer bonding forces. Our study was made on single crystals of TiS_2, HfS_2, HfSSe, and $HfTe_2$ and on pressed crystalline powders of $ZrTe_2$, HfS_2, MoS_2, $MoSe_2$, and WSe_2. Section II contains a discussion of the sample preparation and characterization. Section III deals with crystal structure and group theory. Section IV contains the infrared spectra and the dispersion analysis. Section V contains a discussion of the infrared results and a discussion of bonding in the transition-metal dichalcogenides as well as other AB_2-type crystals.

II. MATERIAL PREPARATION AND CHARACTERIZATION

Single crystals of most of the group-IV *B* chalcogenides were prepared by the chemical vapor-transport method of Schaefer.[8] The elements (metal purity, 99.95%; chalcogen purity, 99.999%) were accurately weighed in the correct stoichiometric ratios (~ 0.01% weighing accuracy) and sealed along with iodine in evacuated quartz ampoules. These samples were heated uniformly to ~ 900 °C for several days followed by transporting for two weeks in temperature gradients of ~ 100 °C. No excess metal or chalcogen was observed and 10–50% of the reactants usually transported. Single crystals of all the group-IV chalcogenides except $ZrTe_2$ could be obtained in this fashion. The crystals were flat hexagonal platelets ranging in thickness from 0.1 to 2 mm and in surface area from 4 mm^2 to 1 cm^2. Chemical analysis was carried out on TiS_2 and HfS_2 and the stoichiometry was confirmed to within 0.8%. Crystalline powders of WS_2, MoS_2, and $MoSe_2$ were prepared in a similar manner.

Pellets pressed from reacted powders of HfS_2, $ZrTe_2$, WS_2, MoS_2, and $MoSe_2$ showed a preferred packing arrangement. Electron-microscope photographs of $2H$ TaS_2 showed that approximately 90% of the crystallites had their c axes aligned within 10 ° of the pellet axis (at least at the surface of the pellet). Additional pellets of WS_2, WSe_2, SnS_2, $CdBr_2$, CdI_2, and PbI_2 were pressed from commercially obtained materials; purity was typically 99.9%.

X-ray–diffraction analysis was carried out using a Picher diffractometer and scintillation counter ($CuK\alpha$ radiation). Extremely sharp lines were obtained for the group-IV B chalcogenides which were found to correspond to the hexagonal $1T$ or CdI_2 structure (space group $P\bar{3}m$). The group-VI B chalcogenides gave very broad reflections indicating a high degree of stacking disorder and were found to be in the hexagonal $2H(b)$ configuration (space group $P6_3/mmc$). Table I lists the observed lattice parameters.

Both the transported crystals and the remaining untransported crystalline powders of the Ti and Hf (including the mixed-anion sample $HfS_{1.0}Se_{1.0}$) compounds showed single phases. This fact together with the chemical analysis indicates that these compounds form very close to the ideal stoichiometry, MX_2. X rays of the Zr compounds, on the other hand, usually showed several phases to be present. ZrS_2 was found to be accompanied by small amounts ($\leq 5\%$) of Zr_4S_3 and ZrS_3. The transported crystals of the Zr-Se sample were almost entirely in the layered hexagonal ($C6$) phase; the untransported powder, however, showed 5–10% of the monoclinic phase $ZrSe_3$. In the Zr-Te sample, the transported crystals were predominantly $ZrTe_3$ while the *un*transported powder was observed to be hexagonal. Gleizes and Jeannin[9] have studied the systems Zr-Se and Zr-Te extensively and report that the hexagonal CdI_2 phase range does *not* extend to the limit ZrX_2 in either of these systems. By comparing our lattice parameters with those reported by Gleizes and Jeannin, we find that our samples were actually of the form $ZrSe_{1.98\pm0.04}$. Vacancies at the chalcogen sites are apparently responsible for the deviation from the stoichiometry ZrX_2.

It should be noted that in preparing the group-IV B chalcogenides samples, a fine white film was usually observed coating the inside surface of the quartz vessel at the reaction (hot) end of the tube. This material, although not present in the x-ray patterns, is undoubtedly the reaction product of the group-IV metal with the silica tube which has been reported by other authors.[9,10]

III. CRYSTAL STRUCTURE AND GROUP THEORY

The materials we are concerned with here are layered crystals which can occur in a variety of stacking arrangements.[11] Our studies are restricted to two structural polytypes, the $1T$ and $2H$ crystals. Figure 1 is a schematic representation of the two crystal structures. If we denote the materials as MX_2 (M = metal atom, X = chalcogenide atom), then the general structure of the materials is shown in Fig. 1(a). Sandwiched layers of the form XMX are separated by a "Van der Waals"-type gap between the X layers of adjacent sheets. In the layers the coordination of the metal ions is either octahedral as indicated in Fig. 1(b) or that of a body-centered-trigonal prism as shown in Fig.

TABLE I. Lattice parameters for layered transition-metal dichalcogenides.

Material MX_2	Coordination (at metal atom)	Lattice parameters (Å) a	c	c/a ratio
Group IV				
TiS_2	octahedral	3.404	5.699	1.674
$TiSe_2$	octahedral	3.542	6.015	1.698
$TiTe_{1.17}$	octahedral	3.768	6.500	1.725
ZrS_2	octahedral	3.661	5.829	1.592
$ZrSe_{1.98}$	octahedral	3.773	6.133	1.625
$ZrTe_{1.76}$	octahedral	3.951	6.627	1.677
HfS_2	octahedral	3.630	5.854	1.612
$HfS_{1.0}Se_{1.0}$	octahedral	3.694	6.061	1.641
$HfSe_2$	octahedral	3.747	6.158	1.643
$HfTe_2$	octahedral	3.951	6.659	1.685
Group VI				
MoS_2	trigonal prism	3.162	12.29	2×1.943
$MoSe_2$	trigonal prism	3.288	12.93	2×1.965
WS_2	trigonal prism	3.162	12.37	2×1.956
WSe_2	trigonal prism	3.286	12.99	2×1.977

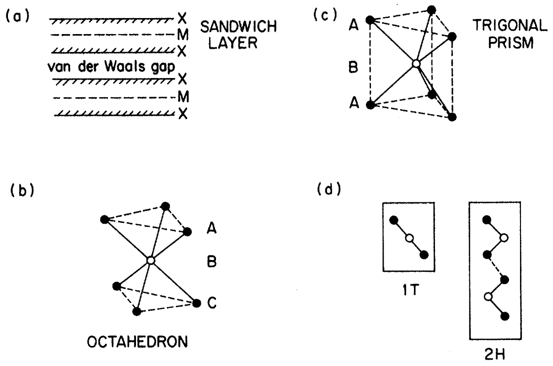

FIG. 1. Schematic representation of the structure of the transition-metal dichalcogenides: (a) the general form of the MX_2 layer structure; (b) octahedral coordination; (c) trigonal-prism coordination; (d) $1T$ and $2H$ polytype structures.

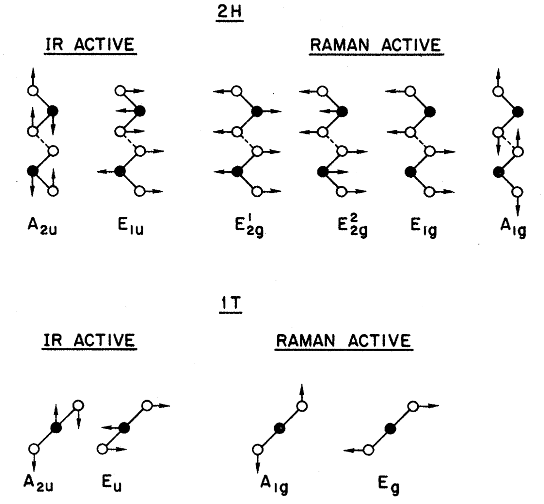

FIG. 2. Displacement vectors for the infrared- and Raman-active modes in the $2H$ and $1T$ polytypes.

1(c). In the trigonal-prism configuration the intralayer structure is of the form *ABA*, whereas in the octahedral configuration it is *ABC*. Figure 1(d) indicates the stacking polytypes of interest in this study. The group-IV (Ti, Zr, Hf) dichalcogenides occur in the $1T$ stacking polytype in which the metal-ion configuration is octahedral. The group-VI (Mo, W,) dichalcogenides occur in the $2H$ stacking polytype in which the metal-ion coordination configuration is a trigonal prism. MoS_2, $MoSe_2$, and WS_2 also occur in another structural polytype, $3R$.[11]

In addition to the values of the lattice parameters c and a, Table I also contains the c/a ratio for the materials under consideration. The c/a ratio is ideally equal to 1.633 for the $1T$ octahedral packing and equal to 2×1.813 for the $2H$ trigonal-prism packing. The ideal $1T$ structure can also be viewed as a defect NiAs structure in which every other plane of Ni atoms has been removed.

A group-theoretical analysis of the Γ-point lattice modes for the $2H$ MoS_2 structure has been given by Verble and Wieting.[12] There are six atoms per unit cell; this gives rise to 18 vibrational modes. These decompose into irreducible representations at the Brillouin-zone center as follows:

$$\Gamma = 2A_{2u} + B_{2g}^1 + B_{2g}^2 + B_{1u} + A_{1g} + 2E_{1u} + E_{2g}^1 + E_{2g}^2 + E_{2u} + E_{1g} \ . \qquad (1)$$

The mode motions for the infrared- and Raman-active optic vibrations are shown in Fig. 2(a). For the $1T$ TiS_2 structure, there are three atoms per unit cell and the decomposition into irreducible representations[13] at the Γ point is given by

$$\Gamma = A_{1g} + E_g + 2A_{2u} + 2E_u \ . \qquad (2)$$

The optic-mode motions are shown in Fig. 2(b). Table II contains the activities of the optic modes for the $2H$ MoS_2 and $1T$ TiS_2 structures. In this work our emphasis will be on the infrared-active modes in which the polarization is in the plane of the layer, i.e., the E_{1u} optic mode for the $2H$ structure and the E_u optic mode for the $1T$ structure.

IV. INFRARED SPECTRA AND OSCILLATOR ANALYSIS

All of the measurements reported in this paper were made on a Perkin-Elmer model No. 180 spectrophotometer. The instrument was operated in a double-beam mode in which the reference was

TABLE II. Symmetries and selection rules for the long-wavelength acoustic and optic phonons in the $1T$ and $2H$ polytype geometries.

	Irreducible representations	Modes at $q=0$ Acoustic	Optic	Selection rules
$1T$ polytypes D_{3d}	A_{1g}	0	1	Raman
	E_g	0	1	Raman
	A_{2u}	1	1	ir (z), $\vec{E} \parallel \vec{c}$
	E_u	1	1	ir (x, y), $\vec{E} \perp \vec{c}$
$2H$ polytypes D_{6h}	A_{2u}	1	0	inactive
	B_{2g}^2	0	1	inactive
	A_{2u}	0	1	ir (z), $\vec{E} \parallel \vec{c}$
	B_{2g}^1	0	1	inactive
	A_{1g}	0	1	Raman
	B_{1u}	0	1	inactive
	E_{1u}	1	0	inactive
	E_{2g}^2	0	1	Raman
	E_{1u}	0	1	ir (x, y), $\vec{E} \perp \vec{c}$
	E_{2g}^1	0	1	Raman
	E_{1g}	0	1	Raman
	E_{2u}	0	1	inactive

a front-surface Al mirror. Measurements at frequencies greater than 500 cm^{-1} were made using a thermopile detector, and measurements in the spectral range 30–500 cm^{-1} were made using a pyroelectric detector. The reflectance was measured at near-normal incidence, ~15°, and at room temperature.

Figures 3–5 contain the reflectance spectra for the single crystals of the group-IV dichalcogenides. Since the crystals were typically thin platelets, spectra could only be obtained for a geometry in which the propagation direction was along the c axis, i.e., we could only study the E_u mode for which the polarization was perpendicular to the c axis. Figure 3 displays the spectra for ZrS_2, HfS_2, and $HfSe_2$ and Fig. 4 displays the spectrum for HfSSe. Figure 5 displays the spectra for TiS_2 and $HfTe_2$. Also included in Fig. 5 is the reflectance for a pressed pellet of $ZrTe_2$. In each case the solid curve is a synthetic reflectivity spectrum obtained from an oscillator model; the dashed lines represent the experimental data.

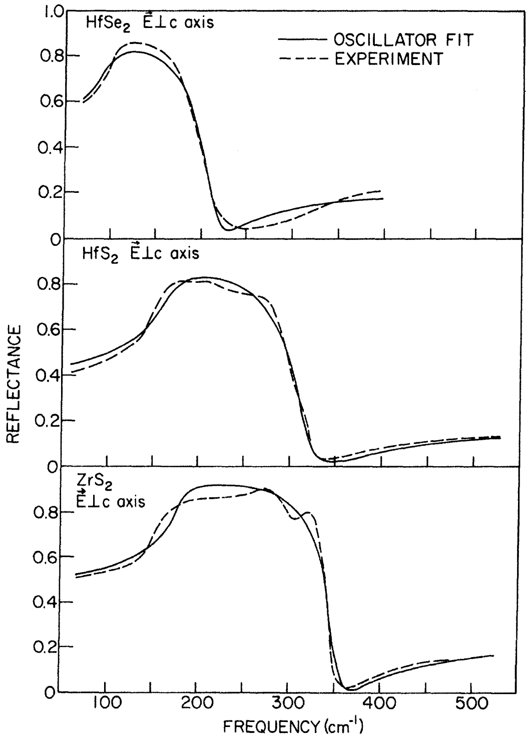

FIG. 3. Room-temperature reflectance spectra for ZrS_2, HfS_2, and $HfSe_2$ for $\vec{E}\perp\vec{c}$ axis. The dashed curves are the experimental data, the solid lines are the dispersion analysis.

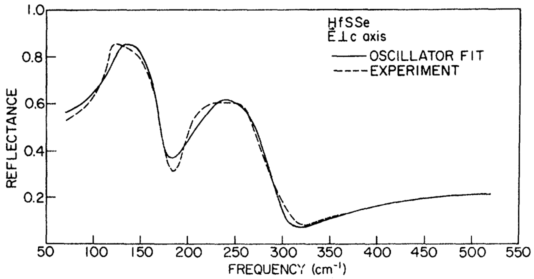

FIG. 4. Room-temperature reflectance spectrum for HfSSe for $\vec{E}\perp\vec{c}$ axis. The dashed curve is the experimental data, the solid line is the dispersion analysis.

An analytical description of the reflectance spectrum was obtained by fitting the data to a reflectance that was constructed or synthesized from a superposition of damped Lorentzian oscillators in which the oscillator frequencies, strengths, and damping were taken as the adjustable parameters. This was done by writing the complex dielectric constant $\epsilon=\epsilon_1+i\epsilon_2$ as

$$\epsilon(\nu)=\epsilon_\infty+\sum_j \frac{S_j\nu_j^2}{\nu_j^2-\nu^2-i\gamma_j\nu_j\nu}\ , \qquad (3)$$

where ϵ_∞ is the high-frequency dielectric constant, ν_j is the oscillator frequency (in cm^{-1}), S_j is the oscillator strength (and is equal to the contribution of the jth oscillator to the static dielectric constant ϵ_0), and γ_j is the damping constant. The synthesized reflectivity is then given by

$$|(\epsilon^{1/2}-1)/(\epsilon^{1/2}+1)^2|\ . \qquad (4)$$

The oscillator parameters were obtained by

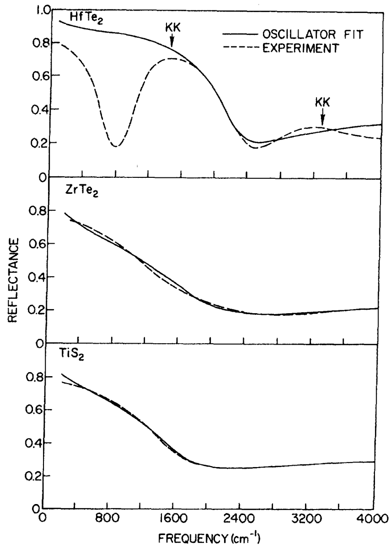

FIG. 5. Room-temperature reflectance spectra for TiS_2, $ZrTe_2$, and $HfTe_2$ for $\vec{E}\perp\vec{c}$ axis. The dash curves are the experimental data, the solid lines are the dispersion analysis. The arrows indicate the frequencies of the additional peaks in ϵ_2 as determined from the Kramers–Kronig analysis.

means of a computer program[14, 15] which performs an iterative search in parameter space. The optimization criterion is the minimization of the rms deviation of the synthesized reflectance from the experimental reflectance. The oscillator-fit parameters for ZrS_2, HfS_2, $HfSe_2$, and HfSSe are given in Table III. Also included in Table III are the rms deviations for each of the fits.

The experimental data in Fig. 5 are not representative of lattice modes, but rather are characteristic of plasmon modes. For the TiS_2 and $ZrTe_2$ the fitting procedure was done with a single mode for which the dielectric constant is of the form

$$\epsilon = \epsilon_\infty - \frac{\omega_p^2}{\omega(\omega + i/\tau)} , \tag{5}$$

where ω_p^2 is the unscreened plasmon frequency, $\omega_p^2 = 4\pi n e^2/m^*$, n is the electron density, m^* is the effective mass, and τ is the scattering time of the free carriers. For $HfTe_2$, there are additional structures which show up as a "hole" in the reflectance spectrum near 800 cm^{-1} and as an additional maximum near 3500 cm^{-1}. An attempt was made to fit the reflectance spectrum of $HfTe_2$ with a dielectric constant of the form

$$\epsilon = \epsilon_\infty + \sum_{i=1}^{2} \frac{S_i \nu_i^2}{\nu_i^2 - \nu^2 - i\gamma_i \nu_i \nu} - \frac{\omega_p^2}{\omega(\omega + i/\tau)} . \tag{6}$$

The best fit that could be obtained using damped Lorentzian oscillators to describe the additional spectral features at ~800 and ~ 3500 cm^{-1} was substantially poorer than the fits obtained for the other materials; the rms deviation for the $HfTe_2$ fit was 9×10^{-2} as compared to 1×10^{-2} for TiS_2. The $HfTe_2$ spectrum was subsequently analyzed using a Kramers-Kronig (KK) dispersion analysis; this procedure indicated the non-Lorentzian character of the "oscillators" which give rise to the additional spectral features. In Fig. 5, we have included a single-plasmon-mode fit to the $HfTe_2$ reflectance; for the synthesized spectrum the fit was made to the leading edge of the reflectance spectrum. The arrows indicate the frequencies of the additional peaks in ϵ_2, as determined from the KK analysis. Our analysis suggests that these spectral features are not vibrational in origin, but rather are associated with electronic transitions. The plasmon-mode fitting parameters for TiS_2, $ZrTe_2$, and $HfTe_2$ are also included in Table III.

Figure 6 contains a comparison of the reflectance spectra for a single crystal of HfS_2 and for a pressed pellet of the same material. Except for the magnitude of the reflectance, the important features of the two curves are the same. In particular, the positions of the leading and trailing edges of the reststrahlen band, which are related, respectively, to the oscillator frequency and the oscillator strength, are essentially coincident. Recall that for the single crystal the spectrum is for the $\vec{E}\perp\vec{c}$ polarization; x-ray measurements indicate a similar alignment of the layered crystallites in the pressed pellets. We can therefore assert that measurements on pressed pellets of these layered crystals will yield spectra from which the oscillator frequencies and strength of the $\vec{E}\perp\vec{c}$ modes can be estimated. Further, if the oscillator strength of the $\vec{E}\perp\vec{c}$ mode is sufficiently weak so that the $\vec{E}\parallel\vec{c}$ reststrahlen band lies outside of the $\vec{E}\perp\vec{c}$ reststrahlen, then it is possible to obtain additional information about the $\vec{E}\parallel\vec{c}$ axis modes from measurements on pressed pellets. This is evidently not the case for HfS_2, but is the case for the group-VI materials as described below.

Figure 7 contains reflectance spectra for a

TABLE III. Dispersion-analysis parameters for the single-crystal dichalcogenides: ZrS_2, HfS_2, $HfSe_2$, HfSSe, TiS_2, $ZrTe_2$, and $HfTe_2$.

Reststrahlen bands

Material	High-frequency dielectric constant ϵ_∞	Phonon frequency ν_0 (cm^{-1})	Oscillator strength S	Damping constant γ	rms dev.
ZrS_2	9.23	181	25.3	0.09	0.036
HfS_2	6.20	166	16.9	0.17	0.028
$HfSe_2$	8.05	98	30.2	0.27	0.032
HfSSe	9.80	122	22.5	0.12	0.025
		219	4.7	0.22	

Plasmon modes

Material	High-frequency dielectric constant ϵ_∞	Plasma frequency ω_p (cm^{-1})	Relaxation time τ (sec)	rms dev.
TiS_2	14.34	6.90×10^3	2.6×10^{-14}	0.011
$ZrTe_2$	9.78	6.37×10^3	2.1×10^{-14}	0.013
$HfTe_2$	20.31	10.34×10^3	5.0×10^{-14}	0.040

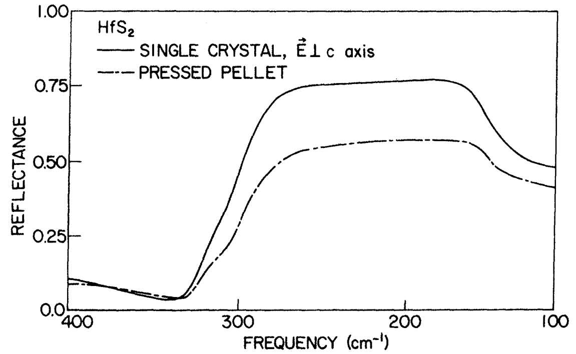

FIG. 6. Comparison of the room-temperature reflectance spectra of a single crystal of HfS_2 ($\vec{E}\perp\vec{c}$ axis) and a pressed pellet.

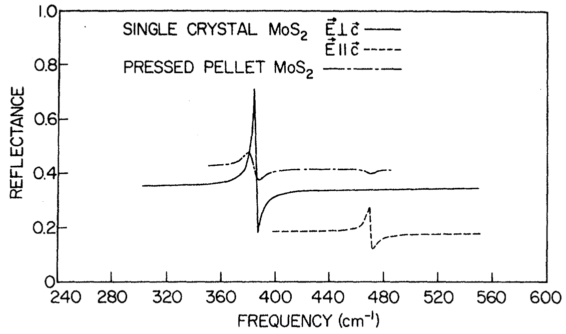

FIG. 8. Room-temperature reflectance spectra for pressed pellets of MoS_2, $MoSe_2$, WS_2, and WSe_2. The arrows indicate the approximate frequencies of the infrared-active optic modes.

pressed pellet of MoS_2 and synthesized reflectance spectra for single-crystal MoS_2. The single-crystal spectra were synthesized from the oscillator parameters given in Ref. 4. As can be seen, the reflectance spectrum of the pressed pellet has two features; the stronger one is coincident with the $\vec{E}\perp\vec{c}$ reststrahlen band of the single crystal and the weaker one is coincident with the $\vec{E}\parallel\vec{c}$ reststrahlen band. Figure 8 gives the reflectance spectra obtained from pressed pellets of MoS_2, $MoSe_2$, WS_2, and WSe_2. In each case two features are evident, the stronger one is assigned to the $\vec{E}\perp\vec{c}$ mode, the weaker one to the $\vec{E}\parallel\vec{c}$ mode. This assignment can be substantiated by using a reduced-frequency scale.

Keyes[16] has demonstrated the usefulness of reduced or dimensionless frequencies and elastic constants in comparisons of the lattice-dynamical properties of the zinc-blende semiconductors. A characteristic optic-mode frequency Ω_0^2 is defined by

$$\Omega_0^2 = e^2/\overline{m}r_0^3 \ , \tag{7}$$

where r_0 is the interatomic distance and $\overline{m}$ is the reduced mass. The reduced frequency of the jth mode, ω_j, is then defined by

$$\overline{\omega}_j^2 = \omega_j^2/\Omega_0^2 \ . \tag{8}$$

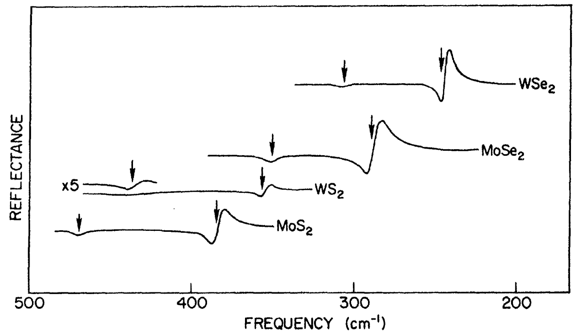

FIG. 7. Comparison of the room-temperature reflectance spectra of a pressed pellet of MoS_2 with the reflectance spectra synthesized from the oscillator-fit parameters of Ref. 4.

In Table IV we give the reduced frequencies for the infrared-active optic modes of MoS_2, $MoSe_2$, WS_2, and WSe_2. For purposes of comparison they are all normalized to the E_{1u} ($\vec{E}\perp\vec{c}$) frequency of MoS_2. The near equality of the normalized reduced frequencies for the $\vec{E}\perp\vec{c}$ modes indicates that the effective force constants in all four materials are very nearly equal. A similar conclusion holds for the $\vec{E}\parallel\vec{c}$ modes. The larger values for the $\vec{E}\parallel\vec{c}$ modes are a result of the unit-cell geometry, i.e., the $\vec{E}\parallel\vec{c}$ mode has a greater degree of bond-stretching character than the $\vec{E}\perp\vec{c}$ mode.

Of primary interest in this paper are the mode strengths or effective-charge parameters of the group-IV semiconducting dichalcogenides ZrS_2, HfS_2, and $HfSe_2$. Figures 9–11 contain plots of ϵ_2 and of the energy-loss function $-\text{Im}(1/\epsilon)$ for ZrS_2, HfS_2, and $HfSe_2$. The positions of the peaks in ϵ_2 locate the frequencies of the TO phonons and the peaks in $-\text{Im}(1/\epsilon)$ locate the frequencies of the LO phonons. These are contained in Table V.

The effective-charge parameter we use in this paper is the macroscopic (or Born) effective charge

TABLE IV. Phonon frequencies and normalized reduced phonon frequencies for MoS_2, $MoSe_2$, WS_2, and WSe_2.

	Phonon frequencies (cm^{-1})		Reduced normalized phonon frequencies	
Material	$\nu(E_{1u})$	$\nu(A_{2u})$	$\overline{\omega}(E_{1u})$	$\overline{\omega}(A_{2u})$
MoS_2	384	470	1.00	1.22
$MoSe_2$	288	350	1.03	1.26
WS_2	356	435	0.99	1.21
WSe_2	245	305	1.01	1.26

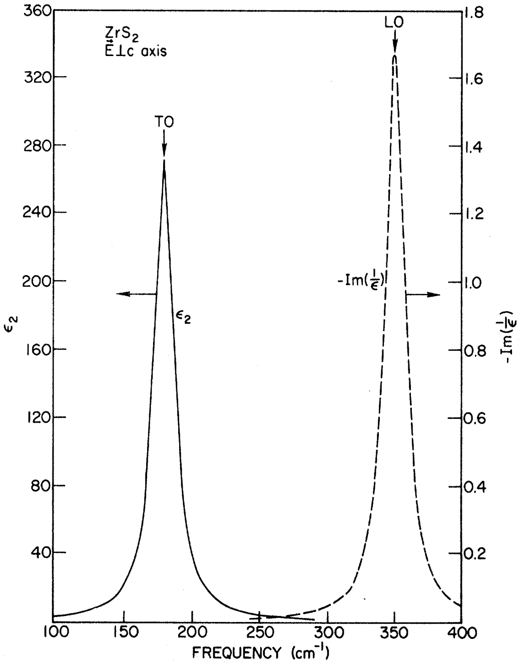

FIG. 9. Frequency dependence of ϵ_2, the imaginary part of the dielectric constant, and $-\mathrm{Im}(1/\epsilon)$, the energy-loss function as synthesized from the oscillator-fit parameters of Table III for ZrS_2. The arrows indicate the TO- and LO-phonon frequencies.

e_T^*; it is defined by

$$e_T^* = \left(\frac{\partial \bar{M}}{\partial \bar{u}}\right)_E , \qquad (9)$$

where $\bar{M}$ is the first-order moment induced by the relative (or optical) displacements of the atoms $\bar{u}$. E is the macroscopic electric field, which is identically equal to zero for the TO phonon. e_T^* can be calculated from the strength of the mode S_j, as determined from the oscillator fit, by the relation

$$\frac{e_T^*}{e} = \frac{\pi^{1/2} c \bar{m}_j^{1/2} S_j^{1/2} \nu_j}{N^{1/2} e} , \qquad (10)$$

where e is the electronic charge, c is the velocity of light, N is the number of oscillators per unit volume, ν_j is the TO-phonon frequency (in cm^{-1}), and $\bar{m}_j$ is the mode mass. For the $1T$ structure $\bar{m}_j$ is obtained from the mode vectors and is given by $m_M m_X/(m_M + 2m_X)$, where m_M is the mass of the metal atom and m_X is the mass of the chalcogenide atom. Table V contains the effective-charge parameters ZrS_2, HfS_2, and $HfSe_2$.

V. DISCUSSION OF INFRARED RESULTS

There are several points that we shall make in this section. The first concerns the very large

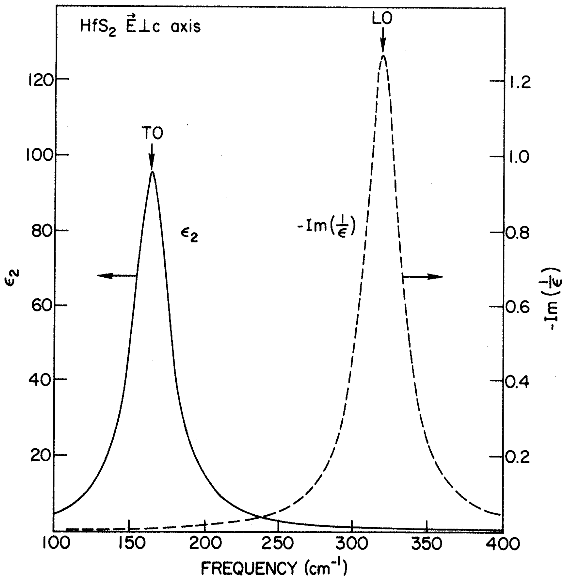

FIG. 10. Frequency dependence of ϵ_2, the imaginary part of the dielectric constant and $-\mathrm{Im}(1/\epsilon)$, the energy-loss function as synthesized from the oscillator-fit parameters of Table III for HfS_2. The arrows indicate the TO- and LO-phonon frequencies.

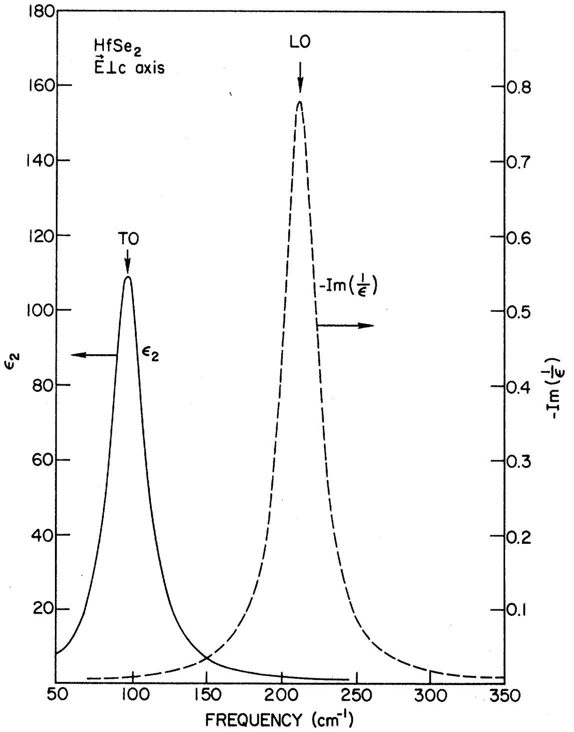

FIG. 11. Frequency dependence of ϵ_2, the imaginary part of the dielectric constant and $-\mathrm{Im}(1/\epsilon)$, the energy-loss function as synthesized from the oscillator-fit parameters of Table III for $HfSe_2$. The arrows indicate the TO- and LO-phonon frequencies.

TABLE V. TO- and LO-phonon frequencies and macroscopic infrared effective charges e_T^*/e for ZrS_2, HfS_2, $HfSe_2$, and HfSSe.

Material	Phonon frequencies (cm^{-1}) TO	LO	Effective charge e_T^*/e
ZrS_2	181	350	4.4
HfS_2	166	318	3.9
$HfSe_2$	98	215	4.3

differences in the reststrahlen bands of the group-IV and -VI semiconducting dichalcogenides. To reemphasize this feature of the data, we have plotted in Fig. 12 the reflectance spectra of MoS_2 and ZrS_2; the large differences in the two spectra are self-evident. The TO-phonon frequency, which occurs at the low-frequency side of the band, is at 384 cm^{-1} in MoS_2 and at 181 cm^{-1} in ZrS_2. Since the atomic masses of Zr (91.22) and Mo (95.94) are almost equal, the large differences in ν_{TO} imply very large differences in the effective forces constants; i.e., if k_{eff} is the force constant, then

$$\omega_{TO}^2 = k_{eff}/\bar{m} \ , \qquad (11)$$

where $\bar{m}$ is the reduced mass. The difference in TO-phonon frequencies implies that the force constants differ by almost a factor of 5. The second point concerns the large differences in the reststrahlen bandwidths, here defined by $\nu_{LO} - \nu_{TO}$. For MoS_2, the bandwidth is approximately 2–3 cm^{-1}, whereas in ZrS_2 it is equal to ~170 cm^{-1}. The reststrahlen bandwidth is related to the oscillator strength of the mode S_j which in turn is proportional to the square of the effective charge e_T^*. On the basis of this comparison the effective charge e_T^* is approximately seven times larger in ZrS_2 than in MoS_2. The large differences in ν_{TO} are consistent with this difference in effective charges if we note that[17,18]

$$\omega_{TO}^2 = \omega_0^2 - f(e_T^*) \ , \qquad (12)$$

where ω_0^2 is a frequency that is characteristic of the effective "spring-constant" force constants of the medium and $f(e_T^*)$ is a reduction in frequency that is related to the interactions between dipole oscillators that reside on the lattice sites. In a point-ion model in which all of the electronic excitations are localized on the lattice sites,[17]

$$f(e_T^*) = \tfrac{4}{3}\pi\,(N e_T^{*2}/\bar{m})\,[3/(\epsilon_\infty + 2)] \ ,$$

whereas in a medium for which the electronic excitations are completely delocalized,

$$f(e_T^*) = \tfrac{4}{3}\pi\,(N e_T^{*2}/\bar{m}) \ .$$

If we denote the factor $\frac{1}{3}(\epsilon_\infty + 2)$ as an effective-field-enhancement factor and further assume that the values of ω_0^2 are essentially the same in both MoS_2 and ZrS_2, then the differences in ω_{TO}^2 are simply attributable to the larger value of e_T^* for ZrS_2. In this case, as expected,[18] the effective-field-enhancement factor is of order unity for both materials.

In the work of Wilson and Yoffe,[11] an attempt was made to account for the optical and electronic properties of a large number of dichalcogenides in terms of a rigid-band model. The model is effective in accounting for many of the features of these compounds; however, it cannot explain why, for example, TiS_2, $ZrTe_2$, and $HfTe_2$ in group IV are metallic rather than semiconducting like HfS_2 and ZrS_2. Within the context of the model, the difference between ZrS_2 and MoS_2 is the occupancy of a lone-pair metal d_{z^2} band in the latter material. As we have already shown, the infrared effective charges in ZrS_2 and MoS_2 differ by a significant factor, $e_T^* = 4.4$ for ZrS_2 and $0.6e$ for MoS_2. It is difficult to account for these large differences in e_T^* in terms of the rigid-band model. A consistent interpretation of the model would give very nearly equal effective charges for the group-IV and group-VI dichalcogenides. The differences we have emphasized in ZrS_2 and MoS_2 extend to all of the group-IV and group-VI semiconducting dichalcogenides; i.e., $e_T^* \sim 4e$ for the group-IV materials and $e_T^* \sim 0.5e$ for the group-VI materials.

There are two mechanisms that can give rise to an infrared effective charge.[19,20] One involves static charge, the other dynamic charge. Recall that the effective charge is defined in terms of the derivative of the dipole moment with respect to the phonon-displacement coordinate. In a rigid-ion model in which the ions are approximated by point charges at the lattice sites, the effective charge is static and is simply related to the formal valence state. For example, if we consider NaCl, and represent it by charges of $+1e$ and $-1e$, respectively, on the Na and Cl sites, then $e_T^* = 1.0e$;

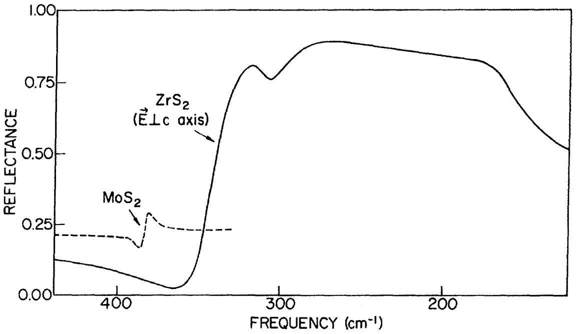

FIG. 12. Comparison of the room-temperature reflectance spectra of a pressed pellet of MoS_2 and a single crystal of ZrS_2 ($\vec{E} \perp \vec{c}$ axis).

for CaF_2, in a similar way, $e_T^* = 2.0e$. One also observes large effective charges in homopolar materials, for example, in trigonal Te, $e_T^* \sim 2.0e$ for the dominant infrared-active modes.[21] For this material the effective charge is dynamic, i.e., it results from charge redistribution which occurs during the execution of a lattice mode. The magnitude of the effective charge is therefore not sufficient for distinguishing the effective-charge mechanism. However, the occurrence of large differences in e_T^* for chemically similar materials, MoS_2 and ZrS_2, is suggestive of significant differences in the chemical bonding.

We note first that the local order in the group-IV and group-VI crystals is different, i.e., in MoS_2 the metal ion is in the body-centered position of a trigonal prism; in ZrS_2 the metal ion is in an octahedral site. This means, in effect, that the effective charge is "structure dependent." In this context it is important to note that the small values of e_T^* in MoS_2-type crystals are not due to a cancellation of terms between the two layers of the unit cell; specifically, whether e_T^* is static or dynamic in origin the contributions from two layers always add. If we carry the structural argument further and examine the intralayer metal-dichalcogenide (M-X) and chalcogenide second-neighbor (X-X) distances, then the origin of the large differences in e_T^* is readily apparent. These crystal distances are given in Table VI along with the sum of ionic radii of the metal and chalcogenide atoms ($M^{4+} + X^{2-}$), and twice the ionic radius of the chalcogenide atom $2X^{2-}$. For ZrS_2, HfS_2, and $HfSe_2$, these interatomic distances (X-M and X-X) are consistent with an ionic description as are the effective charges of order $4e$. For the group-IV materials that we have identified as metallic, TiS_2, $ZrTe_2$, and $HfTe_2$, the interatomic distances are not well described by combinations of ionic radii.

For MoS_2, $MoSe_2$, WS_2, and WSe_2 the ionic description is also inadequate. We concluded above that the bonding in the group-VI semiconducting dichalcogenides was ionic; here we propose that the bonding in the group-VI materials is primarily covalent. The argument for covalency in the group group-VI materials is supported by the fact that the electron configurations about the W ($5d^4 6s^2$) and Mo ($4d^5 5s$) atoms are ideally suited to covalent bonding in a trigonal-prism geometry.[22] In the molecular-orbital picture the bonding configuration in an undistorted trigonal-prism geometry is d^4sp at the metal site and p at the chalcogenide site. These bonding orbitals account for 12 of the 18 electrons. Of the remaining six electrons, four are committed to lone-pair orbitals, one at each S atom in the MoS_2 unit cell. If the last two electrons are put into the d_{z^2} orbitals of the metal atom in the spirit of a rigid-band scheme, this would lead to a large effective charge, $\sim 2e$. We take the small effective charge of the group-VI dichalcogenides to be at variance with such a rigid-band model and to be indicative of covalent bonding between neutral atoms. If one uses the six metal electrons to form covalent bonds, then we suggest that the last two electrons participate in bonding between the S atoms; the small intralayer (X-X) distance in the group-VI materials suggests that there may well be both intralayer and interlayer chalcogenide-chalcogenide atom bonding.

TABLE VI. Comparison of the intralayer anion-anion (X-X) and anion-cation (M-X) distances with ionic radii in several transition-metal dichalcogenides. Also included is the cation-anion radius ratio r^+/r^-. The values in parentheses were obtained from an analysis of the intensities of the diffraction lines (see Table II, Ref. 11), while the others were calculated from a parameter assuming an ideal structure.

Material MX_2	Intralayer X-X (Å)	$2X^{2-}$ (Å)	Intralayer X-M (Å)	$X^{2-} + M^{4+}$ (Å)	r^+/r^- (M^{4+}/X^{2-})
TiS_2	3.40(3.62)	3.68	2.56(2.32)	2.52	0.37
$TiSe_2$	3.54	3.96	2.50	2.66	0.34
$TiTe_2$	3.77	4.42	2.67	2.89	0.31
ZrS_2	3.66	3.68	2.59	2.63	0.43
$ZrSe_{1.92}$	3.77	3.96	2.67	2.77	0.40
$ZrTe_{1.74}$	3.95	4.42	2.80	3.00	0.36
HfS_2	3.63	3.68	2.57	2.62	0.42
$HfSe_2$	3.75	3.96	2.65	2.76	0.39
$HfTe_2$	3.95	4.42	2.80	2.99	0.35
MoS_2	3.16(3.16)	3.68	2.23(2.41)	2.44	0.33
$MoSe_2$	3.29(3.29)	3.96	2.33(2.51)	2.58	0.38
WS_2	3.16	3.68	2.41	2.58	0.30
WSe_2	3.29	3.96	2.51	2.68	0.35

An alternative way of achieving neutral-atom bonding is to compromise on a pure-bonding scheme and fill only four of the six d^4sp metal orbitals with four of the six metal valence electrons and place the other two electrons in the metal nonbonding d_{z^2} orbitals. This would mean that in each "bond" only $\frac{1}{3}$ of the charge density would be associated with the metal while $\frac{2}{3}$ would reside on the chalcogenide. Only a self-consistent band-structure calculation can resolve the relative importance of this scheme and the one described in the paragraph above.

The argument we have just given can be reinforced by comparing the e_T^* values in MoS_2 and β-GaSe. β-GaSe is also a layered compound with a structure similar to MoS_2. For the purposes of our discussion here, the difference in the two materials is in the replacement of the Mo atom by *two* Ga atoms. Wieting and Verble[5] found an effective charge (e_T^*) of $\sim 2.0e$ for β-GaSe. Should this be taken to imply that β-GaSe is ionic? The answer is no. The Ga-Ga and Ga-Se interatomic distances in β-GaSe are completely in accord with a covalent model. However, to achieve covalent bonding in β-GaSe, it is necessary to *transfer* charge from the Se atoms to the Ga atoms; specifically each Ga atom makes four bonds but has only three electrons. Therefore there are at least two components to e_T^* in β-GaSe; a large static component of order $2e$ associated with the formal charge transfer or "ionicity" necessary to achieve a covalent bond and a smaller dynamic component associated with charge redistribution. For MoS_2, the smaller value of e_T^* is taken to imply that there is no formal charge transfer to the lone-pair d orbitals of the Mo atom; thus there is only a small dynamic component in e_T^*. These arguments are supported by electronegativity differences. The small difference between the electronegativities of Ga and Se does not exclude charge transfer to the Ga atoms from the chalcogenide atoms, whereas the larger difference between the electronegativities of the Mo and S atoms does not favor transfer from the S to the Mo atom. In the same way, charge transfer to S or Se atoms from Hf and Zr is favored and is consistent with the ionic bonding we propose.

In β-GaSe, after the bonding and chalcogenide lone-pair orbitals are filled, there are no additional electrons available for other types of interlayer bonding. The arguments we have presented can be further reinforced by comparing the melting points of As_2Se_3 (360 °C) and β-GaSe (960 °C) with the "decomposition" temperature of MoS_2 (1185 °C). In As_2S_3, all of the available valence electrons go into either As-S bonds or into As or S lone-pair orbitals; further, there is no need to invoke a formal charge transfer to account for the electron configuration as indicated above. The relatively low melting point of As_2S_3 is in complete accord with pure van der Waals-type interlayer bonding. The higher melting point of β-GaSe is here attributed to an additional interlayer force of electrostatic origin that is associated with the formal charge transfer that is necessary to satisfy the covalent bonding orbitals. Explicitly the additional interlayer force is a "second"-neighbor-type force between negatively charged metal atoms in one layer and positively charged chalcogenide atoms in the adjacent layers. Finally, the relatively high decomposition temperature of MoS_2 is consistent with the type of interlayer chalcogenide-atom bonding we have suggested above.

One must now account for the occurrence of metallic behavior in TiS_2, $ZrTe_2$, and $HfTe_2$. Here it is convenient to invoke some arguments that are used by physical chemists in describing structure in ionic materials. These arguments have been discussed in detail in another paper.[23] Here we note that in ionic materials, the packing configuration at the cation is a strong function of the radius ratio r^+/r^-, where r^+ is the metal ionic radius and r^- the nonmetal ionic radius. If we consider materials of the form AB_2 which are ionic, where A is the metal, then according to arguments based on the competition between the attraction of unlike ions and the repulsion of like ions, sixfold coordination should prevail at the cation in AB_2 structures for radius ratios between 0.65 and 0.33.[22,24] For radius ratios greater than 0.65 the coordination should be eightfold, whereas for ratios less than 0.33, fourfold coordination is expected. Figure 1 of Ref. 23 shows that this is indeed the trend among the AB_2 crystals. It is interesting to note that the metallic AB_2 crystals TiS_2, $HfTe_2$, and $ZrTe_2$ and the covalent AB_2 crystals, i.e., MoS_2, $MoSe_2$, WS_2, and WSe_2, all possess radii ratios that are very close to 0.33; specifically, they lie between 0.38 and 0.33. For TiS_2, $ZrTe_2$, $HfTe_2$, etc., we have concluded that metallic behavior is associated with the overlap of the X^{2-} p states with the metal s and d states, whereas for the group-VI dichalcogenides, the trigonal prismatic covalent-bonding configuration is a natural consequence of the electron configuration of the metal.[23]

Another point we wish to make concerns the occurrence of two reststrahlen bands in the mixed crystal HfSSe. Here it should be pointed out that in every mixed S-Se material that has been studied to date, two-mode behavior, of the type we report here, has occurred.[25] The systems include crystalline Cd(S, Se) and Zn(S, Se), and amorphous $As_2(S, Se)_3$. The origin of the two-mode behavior is in the relative masses of the S and Se atoms; they are sufficiently different so that in mixed crystals two types of optic modes occur, one in which the S atom vibrates against the metal atom and one in which the Se atom is essentially at rest, and a second mode in which the roles of S and Se are reversed.[26,27]

A final point concerns the analysis of the plasmon-reflectivity modes in TiS_2, $ZrTe_2$, and $HfTe_2$. If one assumes an effective mass of unity, then the free-carrier densities in these materials are all in excess of $10^{20}/cm^3$. The only substantial difference in the three materials is evident in $HfTe_2$, where the τ constant is larger and where there are additional absorption bands. We attribute these and additional bands to electronic transitions associated with the d states of the metal atom.

VI. SUMMARY

We have studied the infrared reflectivity of a large number of the group-IV (Ti, Zr, Hf) and group-VI (Mo, W) dichalcogenides and have observed three distinct types of behavior. ZrS_2, HfS_2, and $HfSe_2$ all display very strong reststrahlen with effective charges of the order of $4e$; TiS_2, $ZrTe_2$, and $HfTe_2$ display a plasmon-reflectivity mode corresponding to carrier densities greater than $10^{20}/cm^3$; and finally, MoS_2, $MoSe_2$, WS_2, and WSe_2 display weak reststrahlen with effective charges of order $0.5e$.

By complementing these infrared results with arguments based on ionic radii and interatomic crystalline distances we have concluded the following.

(i) ZrS_2, HfS_2, and $HfSe_2$ are ionic crystals; we also anticipate ionic bonding in $ZrSe_2$. [Preliminary measurements of the infrared spectrum of a single crystal of $ZrSe_2$ indicate a reststrahlen band in the same spectral region (120–230 cm^{-1}) and of approximately the same strength as that of $HfSe_2$.]

(ii) The bonding in MoS_2, $MoSe_2$, WS_2, and WSe_2 is predominantly covalent.

(iii) TiS_2, $ZrTe_2$, and $HfTe_2$ are metals due to an overlap of the chalcogenide s and p states with the d states of the metal atoms; we anticipate a similar metallic band scheme in $TiSe_2$ and $TiTe_2$. (Initial measurements on single crystals of $TiSe_2$ and $TiTe_2$ indicate that damped-plasmon modes, with plasma frequencies similar to those of TiS_2, dominate the infrared reflectance.)

(iv) The separation of AB_2-type layered crystals into ionic and metallic and covalent crystals is a sensitive function of the radius ratio r^+/r^-; those crystals for which r^+/r^- is greater than ~ 0.38 tend to be ionic, whereas those crystals for which $\sim 0.38 > r^+/r^- > 0.30$ are either metallic or covalent. This last point is substantiated by preliminary measurements we have made on other materials which have layered crystal structure similar or identical to $1T$ TiS_2 (this structure is more commonly denoted as the CdI_2 structure).

Table VII contains a summary of these results; included in the table are the approximate TO- and LO-phonon frequencies, a reduced ratio of these frequencies, $(\nu_{LO}/\nu_{TO})^2 - 1$, which is a measure of the strength of the reststrahlen band, and the radius ratio r^+/r^-. The reduced frequency ratios are of the same order as those for ZrS_2 (2.9), HfS_2 (3.7), and $HfSe_2$ (3.1) and substantially larger than the reduced ratio for covalent AB_2 crystals; for MoS_2, e.g., this ratio is ~ 0.02. Furthermore, the radius ratios are all in excess of 0.38, and the interatomic crystalline distances are well described by combinations of ionic radii. We therefore conclude that these materials, as well as the group-IV semiconducting dichalcogenides, are ionic in nature.

TABLE VII. Approximate LO- and TO-phonon frequencies for $CdBr_2$, CdI_2, PbI_2, and SnS_2. Also included is a reduced ratio of the squares of the phonon frequencies and the cation-anion radius ratio r^+/r^-.

Material	Phonon frequencies (cm^{-1}) LO	TO	$(\nu_{LO}/\nu_{TO})^2 - 1$	r^+/r^-
$CdBr_2$	170	95	2.2	0.50
CdI_2	135	60	4.1	0.45
PbI_2	110	40	6.6	0.56
SnS_2	320	200	1.6	0.39

The large differences in the chemical bonding in the transition-metal dichalcogenides preclude the use of a rigid-band description for this entire class of materials. The ionic-bonding picture we propose for the semiconducting group-IV dichalcogenides is completely in accord with a tight-binding calculation of Murray, Bromley, and Yoffe.[28] In their calculation the valence-band states at Γ are associated with the p states of the chalcogenide atom and the conduction-band states with s and d states of the metal atoms. Our proposal of neutral atom covalent bonding in the group-VI semiconducting dichalcogenides is also in agreement with a tight-bonding calculation of Bromley, Murray, and Yoffe.[29] In their calculation for the group-VI dichalcogenides, the highest-valence-band state at Γ is indeed a d_{z^2} state which is associated with the chalcogenide rather than the metal atoms. As one moves away from Γ this identification becomes more difficult. The assignment of d_{z^2} symmetry character to the top of the valence band is also confirmed by the electron-paramagnetic-resonance measurements of Title and Shafer.[30] Such studies, however, cannot discriminate between d_{z^2} orbitals that are located on the metal or chalcogenide atoms.

ACKNOWLEDGMENTS

The authors wish to acknowledge Dr. T. Geballe and Dr. A. Phillips of Stanford University for stimulating the undertaking of the measurements described in this paper. They also wish to acknowledge the technical assistance of H. Six of Xerox Corporation and M. McClure of Stanford University.

---

[*] Research at Stanford was supported in part by the Air Force Office of Scientific Research under Grant No. AFOSR 68-1510C.

[1] W. P. Omloo and F. Jellinek, J. Less–Common Metals 20, 121 (1970).

[2] F. R. Gamble, F. J. DiSalvo, R. A. Klemm, and T. H. Geballe, Science 168, 568 (1970).

[3] R. Zallen, M. L. Slade, and A. T. Ward, Phys. Rev. B 3, 4257 (1971).

[4] T. J. Wieting and J. L. Verble, Phys. Rev. B 3, 4292 (1971).

[5] T. J. Wieting and J. L. Verble, Phys. Rev. B 5, 1473 (1972).

[6] M. I. Nathan, M. W. Shafer, and J. E. Smith, Jr., Bull. Am. Phys. Soc. 17, 336 (1972).

[7] J. E. Smith, Jr., M. I. Nathan, M. W. Shafer, and J. B. Torrance, The Eleventh International Conference on the Physics of Semiconductors, Warsaw, 1972 (unpublished).

[8] H. Schaefer, *Chemical Transport Reactions* (Academic, New York, 1964).

[9] A. Gleizes and Y. Jeannin, J. Solid State Chem. 5,

42 (1972); 1, 180 (1970).

[10] F. K. McTaggart and A. D. Wadsley, Aust. J. Chem. 11, 445 (1958).

[11] J. A. Wilson and A. D. Yoffe, Advan. Phys. 18, 193 (1969).

[12] J. L. Verble and T. J. Wieting, Phys. Rev. Letters 25, 362 (1970).

[13] P. J. Lockwood, in *Light Scattering in Solids*, edited by G. B. Wright (Springer, New York, 1969), p. 75.

[14] H. W. Verleur, J. Opt. Soc. Am. 58, 1356 (1968).

[15] R. Zallen, G. Lucovsky, W. Taylor, A. Pinczuk, and E. Burstein, Phys. Rev. B 1, 4058 (1970).

[16] R. W. Keyes, J. Appl. Phys. 33, 3371 (1962).

[17] E. Burstein, A. Pinczuk, and R. F. Wallis, in *Proceedings of the Conference of the Physics of Semimetals and Narrow Gap Semiconductors*, edited by D. L. Carter and R. T. Bate (Pergamon, New York, 1971), p. 251.

[18] G. Lucovsky, R. M. Martin, and E. Burstein, Phys. Rev. B 4, 1367 (1971).

[19] E. Burstein, M. H. Brodsky, and G. Lucovsky, Int. J. Quantum Chem. 1S, 759 (1967).

[20] G. Lucovsky, Phys. Rev. B 6, 1480 (1972).

[21] G. Lucovsky, Phys. Status Solidi 49, 633 (1972).

[22] L. Pauling, *The Nature of the Chemical Bond*, 3rd ed. (Cornell University, Ithaca, N. Y., 1960).

[23] R. M. White and G. Lucovsky, Solid State Commun. 11, 1369 (1972).

[24] M. Born and K. Huang, *Dynamical Theory of Crystal Lattices*, (Oxford U.P., London, 1968), pp. 154 ff.

[25] I. F. Chang and S. S. Mitra, Advan. Phys. 20, 359 (1971).

[26] M. Hass, H. B. Rosenstock, and R. E. McGill, Solid State Commun. 7, 1 (1966).

[27] H. Matsuda and T. Miyata, Rept. No. RIFP-79, Research Institute for Fundamental Physics, Kyoto University, 1968 (unpublished).

[28] R. B. Murray, R. A. Bromley, and A. D. Yoffe, J. Phys. C 5, 746 (1972).

[29] R. A. Bromley, R. B. Murray, and A. D. Yoffe, J. Phys. C 5, 759 (1972).

[30] R. S. Title and M. W. Shafer, Phys. Rev. Letters 28, 808 (1972).

PHYSICAL REVIEW B VOLUME 7, NUMBER 8 15 APRIL 1973

Dynamic Effective Charge of a Finite Linear Chain[*]

Stephen L. Cunningham and A. A. Maradudin
Department of Physics, University of California, Irvine, California 92664

(Received 30 March 1972)

A formalism for calculating the dynamic effective charge induced on the atoms of a homopolar crystal by the presence of a surface is presented in the framework of the tight-binding approximation. The method is applied to a one-dimensional chain of two-electron atoms for the purposes of illustration and identification of the critical model parameters. The wave function of the chain is constructed from a linear combination of s-like and p-like atomic orbitals. In the infinite chain, symmetry requires the dynamic effective charge of each atom to vanish. The presence of the free ends in the finite chain, however, induces dynamic effective charges on the atoms which decay in magnitude with increasing distance from the ends. It is found that the important model parameters are the energy band gap and the hopping integral between s and p states centered on adjacent sites. The dependence of the dynamic effective charge on these two parameters is presented.

I. INTRODUCTION

The total dipole moment $\vec{M}$ of a crystal in zero macroscopic electric field can be formally expanded to first order in the displacements of the atoms from their equilibrium positions as[1]

$$M_\alpha = \sum_{lk\beta} M_{\alpha\beta}(lk) u_\beta(lk) \ . \qquad (1)$$

In this expression, $u_\alpha(lk)$ is the α Cartesian component of the displacement from equilibrium of the kth atom in the lth primitive unit cell. The coefficient $M_{\alpha\beta}(lk)$ is an element of the effective charge tensor, and is defined as

$$M_{\alpha\beta}(lk) \equiv \frac{\partial M_\alpha}{\partial u_\beta(lk)}\bigg|_{\vec{u},\vec{E}=0} \ , \qquad (2)$$

where the derivative is evaluated for zero displacements and zero macroscopic electric field.

In infinite crystals having the diamond structure, the coefficients $M_{\alpha\beta}(lk)$ vanish identically due to the following three symmetry conditions: (i) The periodicity of the lattice requires that the coefficients $M_{\alpha\beta}(lk)$ be independent of the cell index l. (ii) The existence of a center of inversion midway between the two basis atoms in every unit cell requires that $M_{\alpha\beta}(lk)$ be the same for the atoms of type $k=1$ and type $k=2$. (iii) The condition that the total dipole moment be invariant against a rigid-body translation gives the sum condition

$$\sum_{lk} M_{\alpha\beta}(lk) = 0 \ . \qquad (3)$$

These three conditions can only be satisfied if all of the coefficients $M_{\alpha\beta}(lk)$ vanish.

In finite crystals, however, conditions (i) and